

1 **Seasonal source variability of carbonaceous aerosols at the Rwanda**  
2 **climate Observatory**

3

4 August Andersson<sup>1</sup>, Elena N Kirillova<sup>1,2</sup>, Stefano Decesari<sup>2</sup>, Langley DeWitt<sup>3</sup>, Jimmy Gasore<sup>3,4,5</sup>,  
5 Katherine E Potter<sup>3</sup>, Ronald G Prinn<sup>3</sup>, Maheswar Rupakheti<sup>6</sup>, Jean de Dieu Ndikubwimana<sup>4</sup>, Julius  
6 Nkusi<sup>4</sup>, Bonfils Safari<sup>5</sup>.

7 <sup>1</sup> Department of Environmental Science and the Bolin Centre for Climate Research, Stockholm  
8 University, SE-10691 Stockholm, Sweden

9 <sup>2</sup> Institute of Atmospheric Sciences and Climate-ISAC, National Research Council of Italy,  
10 Bologna, Italy

11 <sup>3</sup> Center for Global Change Science, Massachusetts Institute of Technology, Cambridge, MA,  
12 USA

13 <sup>4</sup> Climate Secretariat, Ministry of Education, Kigali, Rwanda

14 <sup>5</sup> Physics Department, School of Physics, College of Science and Technology, University of  
15 Rwanda, Kigali, Rwanda

16 <sup>6</sup> Institute for Advanced Sustainability Studies (IASS), Potsdam, Germany

17

18 **Correspondence:** August Andersson (august.andersson@aces.su.se)

19 **Abstract**

20 Sub-Saharan Africa (SSA) is a global hotspot for aerosol emissions, affecting the regional climate  
21 and air quality. In this paper we use ground-based observations to address the currently large  
22 uncertainties in source-resolved emission estimation of carbonaceous aerosols. Ambient fine  
23 fraction aerosol were collected on filters at the high altitude (2590 m.a.s.l.) Rwanda Climate  
24 Observatory (RCO), a SSA background site, during dry and wet seasons in 2014 and 2015. The  
25 concentrations of both carbonaceous and inorganic ion components show a strong seasonal cycle,  
26 with highly elevated concentrations during the dry season. Source marker ratios, including carbon  
27 isotopes, show that the wet and dry seasons have distinct aerosol compositions. The dry season is  
28 characterized by elevated amounts of biomass burning products, approaching ~ 95% for  
29 carbonaceous aerosols. An isotopic mass-balance estimate show that the amount of the  
30 carbonaceous aerosols stemming from savanna fires may increase from  $0.2 \mu\text{g}/\text{m}^3$  in the wet season  
31 up to  $10\mu\text{g}/\text{m}^3$  during the dry season. Taken together, we here quantitatively show that savanna  
32 fire is the key modulator of the seasonal aerosol composition variability at the RCO.

## 33        **1. Introduction**

34        Sub-Saharan Africa (SSA) currently faces major challenges for sustainable development,  
35        including industrial development, agriculture, fresh water supply, climate change, energy  
36        resources and air pollution (IPCC 2014; UNDP, 2018). Either directly, or indirectly, these  
37        challenges are linked to aerosol emissions. Aerosols offset the ongoing regional climate warming  
38        in SSA, shift monsoon and precipitation patterns, and are detrimental for air quality (IPCC 2013;  
39        WHO 2016). Ambient air pollution in SSA is estimated to cause 563.000 premature deaths  
40        annually, making it one of the main causes for mortality in the region (Bauer et al., 2019).  
41        However, the level of scientific understanding of the overall health- and climate impact is still low,  
42        owing to the complex aerosol lifecycle, where emissions, transformations and sinks are associated  
43        with large uncertainties, in particular given their vast physical and chemical complexity. A major  
44        limiting factor for improving our understanding of these effects in SSA are the limited number of  
45        in situ observations (Williams, 2007; Cais et al., 2011; Kulmala, 2018; López-Ballesteros et al.,  
46        2018).

47        A major source of aerosol emissions in SSA are dry season regional fires, clearly visible from  
48        space (Fig. 1). These are occasionally ignited naturally by lightning strikes, but are mainly lit by  
49        humans. There is evidence that slash-and-burn agriculture in SSA has been a common practice for  
50        thousands of years (Bird and Cali, 1998; Archibald et al., 2012). This long-term anthropogenic  
51        perturbation is a significant modulator of current ecosystem structure. A number of studies have  
52        specifically focused on characterizing emissions of aerosols and gases from African fires, e.g., the  
53        Southern African Regional Science Initiative Project (SAFARI 2000), conducted between 1999 to  
54        2001 (Swap et al., 2003). Ground- and airborne chemical characterization from this and other  
55        campaigns suggest a rather distinct aerosol chemical composition, including elevated BC, K<sup>+</sup> and  
56        NO<sub>3</sub><sup>-</sup> concentrations (Table 1).

57        Carbonaceous aerosols, often quantified as total carbon (TC), are generally divided into two main  
58        components: black carbon (BC; here we use elemental carbon (EC) to quantify the amounts of  
59        BC) and organic carbon (OC). Although overlapping to some extent, these two pools generally  
60        have distinct atmospheric lifecycles and environmental effects. Formed from incomplete  
61        combustion, sunlight-absorbing BC contributes to regional warming and is a particularly health  
62        detrimental component in air pollution (WHO 2012; WMO/UNEP 2011; IPCC 2013; Bond et al.,

63 2013). BC is chemically inert to atmospheric reactions, and thus the lifetime is mainly determined  
64 by deposition. OC is also emitted from incomplete combustion (however, with different emission  
65 factors) but is also of non-combustion origins and is formed in the air through secondary processes.  
66 OC is thought to have an overall cooling effect on the climate (IPCC, 2013). Being more  
67 chemically reactive, the OC pool to some extent has a more complex atmospheric lifecycle, with  
68 continuous heterogenous chemistry, rendering the lifetime dependent on both precipitation and  
69 chemical transformations. Emissions from SSA fires are expected to contribute to a significant  
70 part of the global TC atmospheric burden (Lioussé et al., 2015).

71 In general, the actual environmental impact of TC on SSA is poorly constrained. Bottom-up  
72 emission projections suggests that the TC emissions from SSA are expected to increase rapidly  
73 during the coming decades, perhaps reaching 50% of the global burden by 2030 (Lioussé et al.,  
74 2014). To quantify and evaluate such model predictions, as well as to characterize the overall  
75 aerosol composition, it is valuable to conduct measurements at regional background sites. Dual  
76 carbon isotope characterization ( $\Delta^{14}\text{C}$  and  $\delta^{13}\text{C}$ ) of TC at background sites in South and East Asia  
77 and the Arctic has been shown to be a valuable tool for quantitatively constraining the emissions  
78 from different sources (Gustafsson et al., 2009; Andersson et al., 2015; Sheesley et al., 2012;  
79 Kirillova et al., 2014; Winiger et al., 2019).

80 In this paper we present dual carbon isotope constraints of TC, along with chemical  
81 characterization of inorganic ions and different carbonaceous pools, from a study conducted at the  
82 Rwanda Climate Observatory (RCO), during October 2014 to September 2015. A key objective  
83 of the study was to estimate the relative contributions from major TC source categories at this  
84 regionally representative site in the SSA. In particular, we investigate the source variability  
85 associated with the seasonal variations between prevailing wet and dry monsoon seasons in the  
86 region and the contributions from savanna fires.

87

## 88 **2. Methods and Materials**

### 89 **2.1 Field site and regional meteorology**

90 The sampling site, the Rwanda Climate Observatory (RCO), is located on the top of Mt. Mugogo,  
91 in mountainous western Rwanda. (1.586° S, 29.566° E, 2590 m above sea level, 5 m.a.g.l.). The

92 station was established as a collaboration between the Massachusetts Institute of Technology  
93 (MIT, USA) and the Rwandan Government in 2013. The station is described in more detail by  
94 DeWitt et al. (2019). The station is an Advanced Global Atmospheric Gases Experiment (AGAGE)  
95 network site (for full list of instruments see <http://agage.mit.edu>).

96 The meteorology of Rwanda is governed by the East African monsoon, with peak rainfalls in in  
97 April and November. There are thus two dry seasons, December-January-February (DJF) and the  
98 main dry season June-July-August (JAA). The dry seasons in SSA are characterized by extensive  
99 biomass burning. During JJA the fires mainly occur to the south of Rwanda (Fig. 1). Savannas are  
100 the main biomes in SSA, covering ~ 65% of the landmass, and are the main source of fire emissions  
101 (Cahoon et al., 1992). Located in a highly elevated region, Rwanda is, broadly speaking,  
102 surrounded by savanna regions, except to the west, where the tropical rainforests of Africa are  
103 located.

104

## 105 2.2 Filter sampling

106 Quartz filter samples (Millpore, 150 mm diameter) were collected with a high-volume sampler  
107 operating at  $30\text{m}^3\text{h}^{-1}$  using a  $\text{PM}_{2.5}$  inlet (DH-77, Digital Inc. Switzerland). Night-time only (1AM  
108 to 6AM) was conducted to minimize the effects of local emissions and day-time local atmospheric  
109 chemistry and to increase likelihood to capture the regional, free troposphere, signals. This strategy  
110 is supported by high temporal resolution investigations of the diurnal cycle of, e.g., BC (DeWitt  
111 et al., 2019). Each sample was collected over a period of 7 days. The samples were pre-combusted  
112 together with aluminum foil envelopes ( $400^\circ\text{C}$  for 5h), and were treated with special attention to  
113 minimize contamination. The samples were subsequently shipped to Stockholm University for  
114 chemical analysis and isolation for carbon isotope analysis. The samples were stored in freezers  
115 both on site and at Stockholm University. Field blanks were collected on a monthly basis. The  
116 present campaign covers the period October 2014 to September 2015. However, the period  
117 December 2014 to April 2015 is missing due to a lightning strike which damaged the instrument.  
118 Thus, this study presents results from analysis of filter samples (in total 25) collected for the  
119 periods that cover the beginning of the 2014 fall rainy season (Oct-Nov), the end of the spring  
120 2015 rainy season (April – May) and the dry 2015 summer season (June – September). We jointly  
121 refer the October-November 2014 and the April-May 2015 periods as the wet seasons.

122 2.3 Concentrations analysis

123 The concentrations of elemental carbon (EC – mass-based tracer for black carbon) and organic  
124 carbon (OC) were determined using a Sunset Inc. (Tigard, Oregon, USA) thermal-optical  
125 instrument using the NIOSH 4050 protocol (Birch and Cary, 1996; Table S1). Pre-treatment using  
126 acid fumigation with 1M HCl ensured efficient removal of carbonates. A glucose solution was  
127 used to calibrate the FID-response of the instrument, and the long-term performance of the  
128 instrument was checked through running of National Institute of Standards and Technology  
129 (NIST) Standard Reference Materials (SRM) standards. All the concentrations were blank  
130 corrected and the field blank input was on average 2% for OC and 0% for EC. The average relative  
131 standard deviation of the triplicate analysis was 5% for OC, 7% for EC.

132 Water-soluble organic carbon (WSOC) was extracted from filter sub-samples in ultra-pure Milli-  
133 Q water by shaking for 1.5 hours. The extracts were filtered using 0.45 µm cutoff PTFE syringe  
134 filters (Minisart-SRP 10, Sartorius Stedim biotech, Germany). The concentration of WSOC was  
135 quantified in the filtered solutions as the difference between total water-soluble carbon and water-  
136 soluble inorganic carbon using a high temperature catalytic oxidation instrument TOC-5000A  
137 (Shimadzu, Japan). The samples were neither acidified nor purged, to avoid the loss of volatile  
138 organic compounds. The accuracy of the measurement ranges from 7% ( $70 \mu\text{g L}^{-1}$ ) for  $1 \text{ mg L}^{-1}$  of  
139 carbon solution to 3% for concentrations higher than  $2 \text{ mg L}^{-1}$  of carbon (corresponding to  $60 \mu\text{g}$   
140  $\text{L}^{-1}$ ). All the measurements were blank corrected. WSOC field blanks corresponded to an average  
141 0.5%. The average relative standard deviation of the triplicate analysis was 10%.

142 The concentrations of water-soluble inorganic anions were determined by ion chromatography  
143 using a Dionex ICS-2000 system. Anions were separated using an IonPac AG11 2x50 mm Dionex  
144 guard column, IonPac AS11 2x250 mm Dionex separation column and ASRS 300 self-  
145 regenerating suppressor. A solution of KOH was used as eluent. Cations were separated using an  
146 IonPac CG16 3x50 mm Dionex guard column, IonPac CS11 3x250 mm Dionex separation column  
147 and CSRS 300 self-regenerating suppressor. The analysis of cations was performed using 30 mM  
148 solution of MSA as eluent. Field blanks constituted on average 3% of  $\text{NO}_3^-$ , 2% of  $\text{SO}_4^{2-}$  and 1%  
149 of  $\text{NH}_4^+$  and  $\text{K}^+$  ion concentrations. The triplicate analysis showed the average relative standard  
150 deviation of 2% for  $\text{NO}_3^-$  and  $\text{K}^+$ , 5% for  $\text{SO}_4^{2-}$  and 6% for  $\text{NH}_4^+$ .

151

152

## 2.4 Isotope analysis

153 Approximately every second sample ( $n = 12$ ) were selected for carbon isotope ( $\Delta^{14}\text{C}$  and  $\delta^{13}\text{C}$ )  
154 analysis of total carbon ( $\text{TC} = \text{OC} + \text{EC}$ ; Table S1). The filter samples were combusted using the  
155 Sunset analyzer (total carbon protocol) and the evolved  $\text{CO}_2$  was collected in glass vials using a  
156 liquid nitrogen cryo-trap (Andersson et al., 2015). The vials were subsequently shipped to the  
157 National Ocean Sciences Accelerator Mass Spectrometry (NOSAMS) facility at the Woods Hole  
158 Oceanographic Institute (Falmouth, Massachusetts, USA) for analysis of the dual carbon isotope  
159 signatures. The  $\Delta^{14}\text{C}$ -signature was measured using accelerator mass spectrometry (AMS), while  
160 the  $\delta^{13}\text{C}$ -signature was measured using an Isotope Ratio Mass Spectrometer (IRMS).

161

162

## 2.5 Source Apportionment

163 The  $\Delta^{14}\text{C}$ -signature allows the differentiation between the relative contributions of  
164 biogenic/biomass burning and fossil sources. The fraction biogenic/biomass burning ( $f_{\text{bio}}$ ) may be  
165 calculated using isotopic mass-balance ( $f_{\text{fossil}} = 1 - f_{\text{bio}}$ ):

$$166 \quad f_{\text{bio}} = \frac{\Delta^{14}\text{C}_{\text{sample}} - \Delta^{14}\text{C}_{\text{fossil}}}{\Delta^{14}\text{C}_{\text{bio}} - \Delta^{14}\text{C}_{\text{fossil}}} \quad (1)$$

167 The fossil endmember is  $-1000\%$ , as it is completely depleted in  $^{14}\text{C}$ . The biomass endmember is  
168 more complex. For annual plants it is fairly straight-forward: the biomass  $\Delta^{14}\text{C}$ -signature equals  
169 the  $\Delta^{14}\text{C}$  value of  $\text{CO}_2$  for that year ( $\sim +20\%$  for 2014/15, Graven, 2015; Turnbull et al., 2017).  
170 For more long-lived species (e.g., trees) the  $\Delta^{14}\text{C}$ -signature is the average of the atmospheric  $\text{CO}_2$   
171 values (weighted by yearly carbon accumulation) over the plants' lifetime. Bottom-up estimation  
172 of  $\Delta^{14}\text{C}_{\text{bio}}$  therefore requires information regarding the plant distribution in the area of interest, and  
173 the annual bioaccumulation of carbon for the different plants. As an alternative we here use the  
174 combined  $\Delta^{14}\text{C}$ -signature of dissolved organic carbon (DOC) in three of the regions' major rivers,  
175 Congo, Zambezi and Tana, to obtain a regional  $\Delta^{14}\text{C}_{\text{bio}} = +57 \pm 52 \%$ , which is well in the expected  
176 range of a mixture of annual and multi-year plants (Marwick et al., 2015; Wild et al., 2019, Winiger  
177 et al., 2019).

178 The vegetation in SSA may be divided into two main photosynthetic classes: C<sub>3</sub>-plants and C<sub>4</sub>-  
 179 plants, see discussion in Section 3.5. These two groups have distinct δ<sup>13</sup>C-signatures, allowing  
 180 isotope-based separation. We may then resolve three source classes by combining Δ<sup>14</sup>C and δ<sup>13</sup>C:  
 181 C<sub>3</sub>-plants, C<sub>4</sub>- plants and fossil, through isotopic mass-balance (Andersson et al., 2015):

$$182 \begin{pmatrix} \Delta^{14}C(i) \\ \delta^{13}C(i) \\ 1 \end{pmatrix} = \begin{pmatrix} \Delta^{14}C_{C3} & \Delta^{14}C_{fossil} & \Delta^{14}C_{C4} \\ \delta^{13}C_{C3} & \delta^{13}C_{fossil} & \delta^{13}C_{C4} \\ 1 & 1 & 1 \end{pmatrix} \begin{pmatrix} f_{C3}(i) \\ f_{fossil}(i) \\ f_{C4}(i) \end{pmatrix} \quad (2)$$

183 Endmember variability may significantly influence the calculated source fractional contributions  
 184 (Andersson, 2011). For a discussion on the specific endmember ranges used here, see Section 3.5.

185 In Eq. (2) the isotopic data is treated as independent. However, here we find that there is a  
 186 dependence between the isotope ratios and the TC concentrations, such that Δ<sup>14</sup>C(i) ~ A/TC(i) +B,  
 187 where A and B are constants, and i is the sample index (Fig. 5). This is known as a Keeling relation,  
 188 and is discussed in more detail in Section 3.4. The relation holds for both Δ<sup>14</sup>C (R<sup>2</sup>=0.85, p<0.01)  
 189 and δ<sup>13</sup>C, while the correlation is weaker for δ<sup>13</sup>C (R<sup>2</sup>=0.55, p<0.1). A method for using  
 190 correlations within the framework Bayesian source apportionment has recently been developed  
 191 (Martens et al., 2019). The rationale is based on both statistical concepts and the averaging  
 192 expected from atmospheric mixing. The endmember ranges used in the calculations are from  
 193 isolated sources, but during long-range transport the variability within a given source, e.g., savanna  
 194 fires, will be reduced. Using correlations between data points, a means for accounting for the  
 195 mixing is obtained, and more realistic source fraction estimates are obtained. When using the  
 196 estimated source fractions to back-calculate the isotope signatures, the agreement is good  
 197 compared with direct fits (Fig. 5 and Fig. S2). A sensitivity analysis is discussed in section 3.5  
 198 (Fig. S3)

199 To account for the correlations in the data-set we therefore add a second constraint in the source  
 200 apportionment calculations, based on the relation to the TC concentrations:

$$201 \begin{pmatrix} f_{C3}(i) \\ f_{fossil}(i) \\ f_{C4}(i) \end{pmatrix} = \frac{1}{[TC(i)]} \cdot \begin{pmatrix} f_{C3,slope} \\ f_{fossil,slope} \\ f_{C4,slope} \end{pmatrix} + \begin{pmatrix} f_{C3,intercept} \\ f_{fossil,intercept} \\ f_{C4,intercept} \end{pmatrix} \quad (3)$$



202 Where we, instead of fitting a source vector ( $f_{C3}$ ,  $f_{fossil}$ ,  $f_{C4}$ ) for each individual data pair, fit two  
203 vectors: a slope and an intercept of the line, to all data points. This clearly holds the advantage of  
204 have fewer fitting parameters. We emphasize that the strength of the correlation of the isotope  
205 signatures relative to 1/TC is naturally incorporated into this relation, such that lower correlation  
206 of  $\delta^{13}C$  w.r.t 1/TC impose weaker constraints on the calculated source fractions, compared to  $\Delta^{14}C$ .  
207 The source fractions were computed using numerical Markov chain Monte Carlo simulations,  
208 implemented in Matlab, ver. 2015b, using 1000.000 iterations with a burn-in (initial search phase)  
209 of 10.000 and a data thinning of 10 (removing step-wise correlations). The stochastic perturbation  
210 parameter was adjusted as to obtain an acceptance ratio of 0.23, which has been suggested to be  
211 optimal for Metropolis-Hastings algorithms (Roberts et al., 1997). For this set-up, the variability  
212 in the numerically estimated parameters, e.g., the standard deviation of the relative source fraction,  
213 is lower than 1% of the mean value, suggesting good convergence (Winiger et al., 2017).

214

## 215 2.6 Air Mass Back trajectories and Remote Sensing

216 10-days air mass back-trajectories (arrival height 2690 m.a.s.l. (100 m.a.g.l.) and 3090 m.a.s.l.  
217 (500 m.a.g.l.) were calculated using the NOAA Hybrid Single Particle Lagrangian Integrated  
218 Trajectory Model (HYSPLIT) (Figs. 1 and S1). Remote sensing fire-spot detections were retrieved  
219 from the NASA Fire Information for Resource Management Services (FIRMS) database, based on  
220 retrievals from the Moderate Resolution Imaging Spectroradiometer (MODIS) satellite product.

221

## 222 3 Results and Discussion

### 223 3.1 Back-trajectory analysis

224 Air mass back-trajectory analysis show that the air masses arriving at the Rwanda Climate  
225 Observatory (RCO) during the filter collection periods are overall easterly/southeasterly (Figs. 1  
226 and S1). There is some overlap between the wet and boreal summer dry seasons, but overall there  
227 is a seasonal switch, where the wet seasons air masses are more of directly eastern origins (e.g.,  
228 Uganda and Kenya and Tanzania), whereas the dry are more directly southeastern (e.g., Burundi,  
229 Tanzania and Democratic Republic of Congo). During the dry season there are extensive fires to

230 the south of RCO, mainly to the south-west (DR of Congo and Angola). However, the air masses  
231 also pass over regions with comparably high fire activities in the southeast, mainly in Tanzania.  
232 Nevertheless, we emphasize that back-trajectory analysis is challenging in mountainous regions  
233 (e.g., Winiger et al., 2019), and the actual geographical footprints are expected to be broader, e.g.,  
234 due to the propagating effects of turbulence. Here we interpret the back-trajectories qualitatively  
235 to visualize overall air mass transport patterns.

236

### 237 3.2 Concentrations of fine aerosol components

238 During the present campaign, the PM<sub>2.5</sub> carbonaceous and inorganic ion components show a strong  
239 seasonal variability, with elevated levels during the dry JJA season (Fig. 2, Table S1). The dry/wet  
240 season ratios for TC, EC, WSOC, NO<sub>3</sub><sup>-</sup>, SO<sub>4</sub><sup>2-</sup>, NH<sub>4</sub><sup>+</sup> and K<sup>+</sup>, were 4.2, 7.0, 4.1, 12.6, 3.0, 3.2 and  
241 8.8, respectively (Table 1). This variability suggests differences in the aerosol sources and  
242 atmospheric processing, in addition to seasonality in meteorology, e.g., varying boundary layer  
243 heights or precipitation. The sea-salt contributions to the ions are overall estimated to be less than  
244 1%, using corrections with sodium ions (Blanchard and Woodcock, 1980). We here report the  
245 actual concentrations to facilitate direct comparisons with previous studies (Table 1). Overall,  
246 these differences reflect differences in aerosol atmospheric lifetime, air mass transport pathways  
247 and emissions seasonality (e.g., fires). Elevated ratios of EC and K<sup>+</sup> suggests an increased  
248 influence from biomass burning during the dry season. NO<sub>3</sub><sup>-</sup>, which displays the largest seasonal  
249 shift, is often associated with oxidized NO<sub>x</sub> from traffic emissions or lightning strikes. However,  
250 it is also typically elevated in emissions from savanna fires (Table 1; e.g., Gao et al., 2003;  
251 Formenti et al., 2003).

252 The dry season concentrations of carbonaceous aerosols components and inorganic ions reported  
253 here are overall in good agreement with the concentrations observed dry season rural and aged  
254 savanna fire air masses (Table 1). The BC values are in the same range as has previously been  
255 observed at Mt. Kenya ( $0.72 \pm 0.06 \mu\text{gC m}^{-3}$ , Gatari et al., 2003). During atmospheric aging of a  
256 biomass plume, the values of OC, EC and K<sup>+</sup> decrease by a factor of 2-3, whereas other  
257 components are relatively unaffected (Table 1). However, the effects appear variable, as compared  
258 with savanna fires in South Africa (Gao et al., 2003).

259 RCO is situated not far away from the Nyiargongo and Nyamuragria Volcanoes in eastern  
260 Democratic Republic of Congo. High spatial resolution (13x24km<sup>2</sup>) satellite-monitoring of the  
261 SO<sub>2</sub> levels show a near-constant emissions from these volcanoes over the time period covering the  
262 present campaign, likely affecting the observed sulfate levels (Barrière et al., 2017). Here we  
263 observe a spike in sulfate levels (~ 5µg m<sup>-3</sup>) during the week starting of the 13<sup>th</sup> of June 2015 (Fig.  
264 2), but with no clear linkage to an increase in volcanic SO<sub>2</sub> emissions.

265

### 266 3.3 Source marker ratios and correlations

267 Overall, the ratios of different aerosol components provide insights into sources or atmospheric  
268 processes. Here, the EC/TC shows a distinct seasonality (Fig. 3 and Table S1). More commonly  
269 analyzed, though, is the OC/EC ratio (= (TC-EC)/EC), with elevated levels during the wet season  
270 (11±3) compared to the dry season (7±3; Table S1). The OC/EC-ratio is sometimes used as a  
271 marker for biomass burning, but is highly influenced by burning conditions such as flaming or  
272 smoldering fires. In addition, it is highly influenced by atmospheric processes such as secondary  
273 organic aerosol (SOA) formation or photo-chemical aging (e.g., Dasari et al., 2019). The dry  
274 season values observed here are similar to what has been observed in background air at other dry  
275 season Sub-Saharan African sites (Table 1).

276 Similarly, the NH<sub>4</sub><sup>+</sup>/TC and SO<sub>4</sub><sup>2-</sup>/TC are also elevated during the wet seasons (Fig. 3), while  
277 decreasing during the dry seasons, suggesting a different source profile compared to EC, K<sup>+</sup> and  
278 NO<sub>3</sub><sup>-</sup>, including potential volcanic input of SO<sub>2</sub>. In contrast, the WSOC/OC-ratio shows no clear  
279 seasonality, indicating small differences in sources and atmospheric processing of water-soluble  
280 and water-insoluble organic components over the year. TC correlates with K<sup>+</sup> (R<sup>2</sup> = 0.95, p<0.01)  
281 and NO<sub>3</sub><sup>-</sup> (R<sup>2</sup> = 0.95, p<0.01), suggesting that the incomplete combustion regime during the present  
282 campaign is governed by biomass emissions, e.g., savanna burning. Taken together, these ratios  
283 qualitatively suggest that the aerosol regime at RCO is strongly influenced by occasional input of  
284 biomass burning products during the boreal dry season.

285

### 286 3.4 Carbon isotopes

287 Radiocarbon ( $\Delta^{14}\text{C}$ ) and stable-carbon ( $\delta^{13}\text{C}$ ) provides detailed information regarding the sources  
288 and atmospheric processing of carbonaceous aerosols. Here, we investigated the signatures of TC  
289 for roughly every second sample during the campaign. The  $\Delta^{14}\text{C}$ -marker is not influenced by  
290 atmospheric processing, and may be used to directly compute the relative contributions of fossil  
291 vs biomass/biogenic sources with high precision, Eq. (1). The  $\Delta^{14}\text{C}$ -signature show an oscillation  
292 over the seasons, ranging between -84‰ (November, 2014) and +30‰ (July, 2015) (Fig. 4 and  
293 Table S1). Thus, during the JJA season, the  $\Delta^{14}\text{C}$ -signature exceed the signature for atmospheric  
294  $\text{CO}_2$  (+20‰, Graven, 2015; Turnbull, 2017).

295 Using Equation (1), the percentage biomass/biogenic TC for the  $\Delta^{14}\text{C} = +30\text{‰}$  sample is 97%.  
296 During the wet season, the percentage derived from fossil reaches 13%, possibly of a more local  
297 derivation.  $\Delta^{14}\text{C}$  correlates with  $1/\text{TC}$  ( $R^2 = 0.85$ ,  $p < 0.01$ ), which suggests that the variability in  
298 concentrations can be explained as a two-component mixture: a stable background and a  
299 temporally fluctuating source (Keeling, 1958) (Fig. 5A). This inverse relation gives  $\Delta^{14}\text{C} = +37 \pm$   
300  $6\text{‰}$  as TC approaches infinity, showing that the non-background component is of  
301 biogenic/biomass burning origins. The  $\Delta^{14}\text{C}$  signatures for TC reported here are overall higher  
302 than for monitoring sites in South and East Asia (Sheesley et al., 2012; Kirillova et al., 2014;  
303 Bikkina et al., 2016).

304 In contrast to  $\Delta^{14}\text{C}$ , the  $\delta^{13}\text{C}$ -value is influenced by both atmospheric processes (i.e., kinetic isotope  
305 effects, KIE) and source signatures. Here, the  $\delta^{13}\text{C}$ -value shows a similar pattern relative to the  
306  $\Delta^{14}\text{C}$ -value, depleted in  $^{13}\text{C}$  (min  $\delta^{13}\text{C} = -27\text{‰}$ ) during wet seasons, and higher during the dry  
307 season (max  $\delta^{13}\text{C} = -21 \text{‰}$ ) (Fig. 4B). The correlation w.r.t.  $1/\text{TC}$  ( $R^2=0.55$ ,  $p < 0.1$ ) is weaker  
308 compared to  $\Delta^{14}\text{C}$  (Fig. 5B). The direct fossil vs biomass source correlation from the  $\Delta^{14}\text{C}$  Keeling  
309 curve is also driving the  $\delta^{13}\text{C}$ -signatures, but the higher variability is explained by larger  
310 endmember variability and potential influence of KIE, see Section 3.5. An overall enrichment in  
311  $^{13}\text{C}$  has been found in aged air masses in South Asia, especially for WSOC (Kirillova et al., 2013;  
312 Dasari et al., 2019), but less so for TC. In fact, the enrichment of  $^{13}\text{C}$  in WSOC often appears to  
313 be counter-acted by a decrease in water-insoluble OC (e.g., Yan et al., 2017; Fang et al., 2017).

314 The TC  $\delta^{13}\text{C}$  values, and their seasonal trend, are similar to what has previously observed in fine  
315 aerosols at a rural site in Tanzania (May – August, 2011, Mkoma, et al., 2014). However, the

316 temporal trend appears shifted in the RCO samples from values around -25 ‰ to around 22 ‰ in  
317 mid-May. At the Tanzanian site, a similar shift occurs in mid-June. In addition to the complications  
318 of comparing measurements conducted at different sites during different years, there is a good  
319 agreement in the  $\delta^{13}\text{C}$ -values, and the temporal offset may be explained by inter-tropical  
320 convergence zone position variability. Similarly, the  $\delta^{13}\text{C}$ -value for TC at a savanna woodland site  
321 in Zambia, observed during August-September 2000, was  $-21.8 \pm 0.8$  ‰ (Billmark et al., 2003),  
322 while values between -19.3 and  $-23.6$  ‰ were observed at sites in the Ivory Coast (Cachier et al.,  
323 1985).

### 324 3.5. Carbon isotope-based source apportionment

325 By combining the  $\Delta^{14}\text{C}$  and the  $\delta^{13}\text{C}$ -values we can by isotopic mass balance resolve three major  
326 sources of TC at the RCO, Eq. (2). However, there are some important considerations to this  
327 approach: First, the  $\delta^{13}\text{C}$ -value is not an exclusive source marker, but is also affected by  
328 atmospheric processing (e.g., photo-chemical oxidation and secondary formation). Second, the  
329 main source categories must be defined and distinguishable using carbon isotopes. Third, the  
330 source-values of the isotope-signatures, the endmembers, and their natural variability need to be  
331 established.

332 As mentioned, the  $\delta^{13}\text{C}$ -value of bulk TC appears to be considerably less affected by atmospheric  
333 processing compared to sub-components, such as WSOC. Here, the temporal variation of the  $\delta^{13}\text{C}$ -  
334 value is qualitatively similar to that of  $\Delta^{14}\text{C}$ -value (Fig. 4). Since  $\Delta^{14}\text{C}$  is not affected by  
335 atmospheric reactions, this suggests that source variability is a key driver of the  $\delta^{13}\text{C}$  variability.  
336 Furthermore, the WSOC/OC is virtually constant throughout the year (Fig. 3); the WSOC/OC has  
337 been found to be highly affected by atmospheric processing and related to shifting  $\delta^{13}\text{C}$  (Kirillova  
338 et al., 2013; Yan et al., 2017; Fang et al., 2018; Dasari, 2019). Here, we therefore assume that the  
339  $\delta^{13}\text{C}$ -ratio of TC is not strongly perturbed by atmospheric processing during long-range transport,  
340 and may thus be used as a source marker. Nevertheless, we explore the potential influence on KIE,  
341 as well as endmember variability, on the source apportionment results in a sensitivity analysis.

342 Turning to potential sources, there is a multitude of potential source categories for TC in SSA.  
343 However, many of these fall in broad categories, with similar carbon isotope signatures. Around  
344 the world, the applications of dual carbon isotope source apportionment techniques in ambient TC

345 mainly identified/considered 6 broad source categories: C<sub>3</sub> plants, C<sub>4</sub> plants, liquid fossil fuels  
346 (e.g., traffic), coal combustion (solid fossil), gas flaring (gaseous fossil) and marine emissions  
347 (Winiger et al., 2019; Andersson et al., 2015; Kirillova et al., 2013). Overall, the practice of coal  
348 combustion in SSA is expected to be much less frequent than in, for example, South and East Asia,  
349 and we therefore do not consider this source further. In addition, marine emissions are not expected  
350 to have a large influence at RCO, supported by the low estimates of marine contributions to the  
351 inorganic ions (<1%). For gas flaring, there are potential distant sources around the Arabian  
352 Peninsula and off the west coast of Africa, in the Gulf of Guinea. However, given the distances to  
353 the RCO station and the prevailing wind directions, emissions from flaring are not expected to  
354 affect the site, while the  $\delta^{13}\text{C}$ -signatures for gas-flaring are strongly depleted in  $^{13}\text{C}$  ( $\delta^{13}\text{C} < -38\text{‰}$ ;  
355 Winiger et al., 2017) and even a small contribution would shift the observed values significantly.

356 The remaining three main source categories are the two biomass sources of C<sub>3</sub> (e.g., trees) and C<sub>4</sub>  
357 plants (e.g., sugarcane and certain grasses) and liquid fossil fuels (Fig. 6). Aerosols from liquid  
358 fossil fuel sources have a  $\Delta^{14}\text{C}_{\text{fossil}} = -1000\text{‰}$  (completely depleted in  $^{14}\text{C}$ ) and a  $\delta^{13}\text{C}_{\text{fossil}} = -$   
359  $25.5 \pm 1.3\text{‰}$  (Widory, 2006; Andersson et al., 2015). The  $\Delta^{14}\text{C}$  of biomass was established in  
360 Section 2.4 as  $\Delta^{14}\text{C}_{\text{C3}} = \Delta^{14}\text{C}_{\text{C4}} = +57 \pm 52\text{‰}$ . The  $\delta^{13}\text{C}$  of C<sub>3</sub>-plants in general is  $-27.1 \pm 2\text{‰}$   
361 (Bender, 1971; O'Leary, 1988). However, for aerosols generated from C<sub>3</sub>-plants this value may be  
362 either enriched (e.g.,  $\sim 0.5\text{‰}$  biomass burning) or depleted (e.g.,  $\sim 0$  to  $4\text{‰}$  during SOA formation)  
363 (Turekian, 1998; Das et al. 2010, Mkoma et al., 2014; Aguilera and Whigham, 2018). In any case,  
364 the numerical spread in the  $\delta^{13}\text{C}$ -value of these different sources are largely overlapping with that  
365 of the raw materials, and we therefore use this value here. The  $\delta^{13}\text{C}$  of C<sub>4</sub>-plant materials is  $-$   
366  $13.1 \pm 1.2\text{‰}$  (Bender, 1971; O'Leary, 1988; Turekian 1998). However, during incomplete  
367 combustion, the  $\delta^{13}\text{C}_{\text{C4}}$  may be reduced by a factor ranging from 0 to  $7\text{‰}$ , largely dependent on  
368 burning conditions and species (Martinelli, 2002; Das et al., 2010; Aguilera and Whigham, 2018).  
369 Accounting for such effects in source apportionment is a challenge, especially since the reported  
370 values are ranges and not mean and variability, and thus are highly influenced by potential outliers.  
371 We here use a method discussed in Andersson et al. (2015) to address the issue of statistical  
372 analysis of ranges by assuming that the total range corresponds to the 95% confidence intervals of  
373 a normal distribution. This corresponds to the range of 4 times the standard deviation, yielding  $\sigma$   
374  $= 7/4\text{‰}$ , while the mean is  $-7/2\text{‰}$ . Combining this with the variability of the of pure C<sub>4</sub>-plants we

375 obtain:  $\delta^{13}\text{C}_{\text{C4}}: -16.6 \pm 2.2\%$ , where  $\sigma^2 = 1.2^2 + (7/4)^2 \text{‰}^2$ . These values are also what is obtained  
376 by numerical estimation of the convolution of a normal distribution ( $\mu = -16.6$ ,  $\sigma = 1.2\%$ ) with a  
377 uniform distribution ( $[-7, 0] \text{‰}$ ), adding to the strength of statistical representation.

378 The fractional source contributions of fossil fuel,  $\text{C}_3$  and  $\text{C}_4$  to TC are computed with Eqs. (2) and  
379 (3) (Fig. 7). It is well-established that accurate estimation of the fractional source contributions  
380 requires explicit incorporation of the endmember variability, and we here use a Bayesian  
381 framework driven by Markov chain Monte Carlo simulations for this purpose (Andersson, 2011;  
382 Andersson et al., 2015). To estimate the influence of the intra-endmember mixing during  
383 atmospheric transport we use the correlations of the isotopes with TC within the Bayesian  
384 framework, see section 2.5, to account for the endmember averaging during atmospheric transport  
385 (Martens et al., 2019) (Fig. 5). The resulting fractional contributions display a large variability  
386 when comparing wet and dry conditions (Fig. 7A and Table S2). The dry season is characterized  
387 by relatively higher  $\text{C}_4$ -plant contributions, whereas the relative contributions of fossil fuels and  
388  $\text{C}_3$ -plants increase during the wet seasons. Back-calculating the isotope signatures from the  
389 computed source fractions from the MCMC-simulations essentially reproduce the Keeling  
390 relations relative to  $1/\text{TC}$  (Figs. 5 and S2). To check influence of the number of data points used  
391 in the Keeling-based MCMC, we computed comparative scenarios where every third data point  
392 was used (starting at data point 1, 2 and 3 respectively) (Fig S3). The standard deviations for the  
393 calculated  $f_{\text{C3}}$  are on average doubled when only every third point are used (5% vs 10%), showing  
394 how correlations between multiple data points aids in constraining the sources.

395 Since the  $\delta^{13}\text{C}$  endmembers for, in particularly  $\text{C}_4$ -plants, are not well-constrained, we also  
396 employed a sensitivity analysis w.r.t. endmembers and the potential influence of KIE (Tables S2  
397 – S5 and Figs. S4 – S6). In addition to the above discussed best estimate scenario, we tested two  
398  $\delta^{13}\text{C}_{\text{C4}}$  scenarios: a ‘minimum KIE scenario’ with zero KIE ( $\delta^{13}\text{C}_{\text{C4}} -13.1 \pm 1.2\%$ ) and a ‘maximum  
399 KIE scenario’, with a depletion by 5.9‰ ( $\delta^{13}\text{C}_{\text{C4}} -19.0 \pm 2.2\%$ ). The maximum KIE scenario was  
400 established such as the  $f_{\text{C4}}/(f_{\text{C4}}+f_{\text{C3}})$ -ratio would be 62% as TC approach infinity, and thus 100%  
401 savanna contributions, see Eq. (4). As expected, these scenarios significantly shift the estimated  
402 relative  $\text{C}_4$  contributions, resulting in a total range of the sample period averages of 24% (min-  
403 KIE; min 6% max 32%) to 42% (max-KIE; min 10%, max 58%), thus providing lower and upper  
404 bounds (Figs. S4 and S5 and Tables S3 and S4). The corresponding value for our best estimate is

405 32% (max 44%, min 8%). In addition, we investigated a scenario with a 3‰ depletion of the fossil  
406 endmember ( $\delta^{13}\text{C}_{\text{fossil}} -28.5\pm 1.3\text{‰}$ ). Since the fossil contribution is overall low as determined by  
407  $\Delta^{14}\text{C}$ , and since  $\Delta^{14}\text{C}$  constrains the fossil contribution independently of the  $\delta^{13}\text{C}$  data, this shift  
408 has no significant influence on the computed source fractions 6% (max 11%, min 3%) (Fig. S6  
409 and Table S5). Overall, we stress that these three sensitivity test scenarios represent extreme limits,  
410 and the a priori least biased scenario is the initially outlined best scenario.

411 By combining the estimated fractional source contributions with the TC concentrations, we can  
412 estimate the concentrations from the different sources (Fig. 7B), revealing a more accentuated  
413 source variability. The average dry-to-wet ratios of the TC to C<sub>3</sub>-plants, C<sub>4</sub>-plants and fossil fuels  
414 are 3, 5 and 2, respectively.

415 Savannas are the main biome supporting C<sub>4</sub>-plants in SSA. For East African savannas,  $\delta^{13}\text{C}$  data  
416 suggests that  $\sim 62\%$  ( $f_{\text{C}_4,\text{NPP}}$ ) of the net primary production (NPP) is from C<sub>4</sub>-plants (the rest mainly  
417 C<sub>3</sub>-plants, Lloyd et al., 2008). Thus, one may assume that the source characteristics of TC emitted  
418 from savanna burning should represent this plant-signature distribution. However, the aerosol  
419 emissions modulate the NPP activity through emission factors (EF). The uncertainties of EFs from  
420 different biomass burning activities are generally large and overlapping (Andreae, 2019). As a first  
421 approximation, we here use  $f_{\text{C}_4,\text{NPP}}$  to estimate the fractional contribution of savanna emissions to  
422 TC ( $f_{\text{savanna}}$ ) as ( $i$  = sample index):

$$423 \quad f_{\text{savanna}}(i) = \frac{f_{\text{C}_4}(i)}{f_{\text{C}_4,\text{NPP}}} \quad (4)$$

424 This analysis shows that the dry season carbonaceous aerosol regime is dominated by savanna fire  
425 emissions reaching up to 71% (Fig. 7 and Table S2). These results agree with the elevated levels  
426 of EC, K<sup>+</sup> and NO<sub>3</sub><sup>-</sup> during the dry season (Table S1).

427

## 428 5. Outlook

429 In this paper we find that the aerosol composition of the emissions affecting the Rwanda Climate  
430 Observatory (RCO) may be described as a two-state source mixture: a regional/local background  
431 signal modulated by savanna fire emissions. Multiple studies have shown that savanna fires  
432 strongly influence the aerosol regime in SSA. Here, we estimate the savanna fire contributions for



433 carbonaceous aerosols to range from 13% (wet season;  $TC_{\text{savanna}} = 0.2 \mu\text{g m}^{-3}$ ) to 71% (dry season;  
434  $TC_{\text{savanna}} = 9.7 \mu\text{g m}^{-3}$ ) at RCO (Fig. 7). The savanna fires are believed to be mainly lit by humans,  
435 and although these activities have been ongoing perhaps throughout the Holocene, these  
436 anthropogenic activities strongly perturb the regional ecosystems, climate and air quality (e.g.,  
437 Bird and Cali, 1998; Archibald et al., 1998). The annual SSA savanna carbon budget represents a  
438 net  $\text{CO}_2$  source to the atmosphere (Williams, 2007; Cais et al., 2011; Valentini et al., 2014; Palmer  
439 et al., 2019). Finding more sustainable alternatives to the slash-and-burn practices in SSA could  
440 therefore possibly turn the region into a carbon sink. For instance, implementation of early dry  
441 season burning may be a possible strategy (Lipset-Moore et al., 2018). Savanna fire mitigation  
442 would also improve the regional air quality and stabilize precipitation patterns (Hodnebrog et al.,  
443 2015; Heft-Neal et al., 2018; Bauer et al., 2019).

444 Nevertheless, the current level of scientific understanding of the impact of savanna burning on the  
445 environmental system is poor, as are the couplings/responses to climate change, population  
446 growth, urbanization and other key socio-economic and environmental challenges for sustainable  
447 development in SSA (e.g., IPCC, 2014; Lioussé et al., 2015; Brandt et al., 2017; UNDP, 2018).  
448 Savanna burning mitigation, or shifts in in fire regime due to climate change, may change the  
449 present steady-state in unpredictable ways (e.g., Abreu et al., 2017). To better constrain the  
450 multiple environmental impacts of savanna burning in SSA, the comparably few ongoing ground-  
451 based in situ observations should be expanded and solidified (Williams, 2007; Cais et al., 2011;  
452 Kulmala, 2018; López-Ballesteros et al., 2018). For instance, observations of source-segregated  
453 aerosol concentrations provides multiple opportunities for advancing our knowledge of  
454 environmental processes relevant to SSA, including providing means for testing chemical-  
455 transport models; examining the relative importance of cooling vs warming (e.g., BC) aerosols;  
456 ground-truthing remote sensing products and detailed monitoring of the expected rapid change  
457 over the coming decades, including the effects of climate warming, population growth and  
458 urbanization.

459

460 *Data availability:* The chemical and isotopic data, as well as the MCMC-derived relative source  
461 contributions of  $\text{C}_3$ -plants,  $\text{C}_4$ -plants and fossil, and the corresponding source-segregated TC  
462 concentrations is provided in the supplementary information.

463

464 *Competing interests:* The authors declare that they have no conflict of interest.

465

466 *Author contributions:* AA wrote the manuscript, set-up the PM<sub>2.5</sub> high-volume sampler at RCO,  
467 and analyzed the data. ENK and SD conducted the carbonaceous aerosol quantifications and  
468 isolations for isotopes, and IC analysis. JG worked with the instruments, including helping or  
469 leading installation, and provided feedback on data analysis. KEP was instrumental in setting up  
470 the RCO and did most of the initial instrument installation. HLD served as the RCO station chief  
471 scientist for three years. JN and JdDN worked as technical coordinators of the project at different  
472 times and facilitated the operations of the station as well as providing feedback on analysis. BS  
473 was our University of Rwanda liaison as the head of the Master's program in atmospheric and  
474 climate science. RGP is the head of the AGAGE network and is the MIT liaison to the RCO, and  
475 was essential in the setup of the observatory and scientific analysis. All authors commented on the  
476 manuscript.

477

478 *Acknowledgements.* We thank the generous MIT alumni donors to the MIT-Rwanda Climate  
479 Observatory Project and the MIT Center for Global Change Science. We also thank the  
480 Government of Rwanda and the Rwanda Ministry of Education. We also wish to acknowledge the  
481 essential contributions of the Mugogo station technical experts Theobard Habineza, Modeste  
482 Mugabo, Olivier Shyaka, and Gaston Munyampundu and RBA technician Yves Fidele, without  
483 which running this station would be impossible. AA acknowledges project grants from the  
484 Swedish Research council (projects 348-2013-114 and 2017-05687). ENK acknowledges the  
485 People Programme (Marie Curie Actions) of the European Union's Seventh Framework  
486 Programme (FP7/2007-2013) under REA grant agreement 623386. We acknowledge the use of  
487 data and imagery from LANCE FIRMS operated by NASA's Earth Science Data and Information  
488 System (ESDIS) with funding provided by NASA Headquarters. The authors gratefully  
489 acknowledge the NOAA Air Resources Laboratory (ARL) for the provision of the HYSPLIT  
490 transport and dispersion model and/or READY website (<http://www.ready.noaa.gov>) used in this  
491 publication.

492 **References**

- 493 Abreu, R.C., Hoffmann, W.A., Vasconcelos, H.L., Pilo, N.A., Rossatto, D.R., Durigan, G.: The  
494 biodiversity cost of carbon sequestration in tropical savanna. *Sci. Advan.* 3, doi:  
495 10.1126/sciadv.1701284, 2017.
- 496 Aguilera, J., Whigham, L.D.: Using the  $^{13}\text{C}/^{12}\text{C}$  carbon isotope ratio to characterize the emission  
497 sources of airborne particulate matter: a review of literature. *Isotopes Environ. Health. Stud* 54,  
498 573-587, doi: 10.1080/10256016.2018.1531854, 2018.
- 499 Andersson, A.: A systematic examination of a random sampling strategy for source apportionment  
500 calculations. *Sci. Tot. Environ.* 412-413, 232-238, doi: 10.1016/j.scitotenv.2011.031, 2011.
- 501 Andersson, A., Deng, J., Du, K., Zheng, M., Yan, C., Sköld, M., Gustafsson, Ö.: Regionally-  
502 varying combustion sources of the January 2013 severe haze events over Eastern China. *Environ.*  
503 *Sci. Technol.* 49, 2038-2043, doi: 10.1021/es503855e, 2015.
- 504 Andreae, M.O.: Emission of trace gases and aerosols from biomass burning – An updated  
505 assessment. *Atmos. Chem. Phys. Discuss.* doi: 10.5194/acp-2019-303, 2019.
- 506 Archibald, S., Staver, A.C., Levin, S.A.: Evolution of human-driven fire regimes in Africa. *Proc.*  
507 *Nat. Acad. Sci.* 109, 847-852, doi: 10.1073/pnas.1118648109, 2012.
- 508 Aurela, M., Beukes, J.P., van Zyl, P., Vakkari, V., Teinilä, K., Saarikoski, S., Laakso, L.: The  
509 composition of ambient and fresh biomass: burning aerosols at a savannah site, South Africa.  
510 *South Afr. J. Sci.* 112, 1-8, doi: 10.17159/sajs.2016/20150223, 2016.
- 511 Barrière, J., Oth, A., Theys, N., d'Oreye, N., Kervyn, F.: Long-term monitoring of long-period  
512 seismicity and space-based  $\text{SO}_2$  observation at African lava lake volcanoes Nyiarango and  
513 Nyamulagira (DR Congo). *Grophys. Res. Let.* 44, 6020-6029, doi: 10.1002/2017GL073348, 2017.
- 514 Bauer, S.E., Im, U., Mezuman, K., Gao, C.Y.: Desert dust, industrialization, and agricultural fires:  
515 health impacts of outdoor air pollution in Africa. *J. Geophys. Res.* 124, 4104-4120, doi:  
516 10.1029/2018JD029336, 2019.

517 Bender, M.M.: Variations in the  $^{13}\text{C}/^{12}\text{C}$  ratios of plants in relation to the pathway of  
518 photosynthetic carbon dioxide fixation. *Phytochem.* 10, 1239-1244, doi: 10.1016.S0031-  
519 9422(00)84324-1, 1971.

520 Bikkina, S., Andersson, A., Sarin, M.M., Sheesley, R.J., Kirillova, E., Rengarajan, R., Sudheer,  
521 A.K., Ram, K., Gustafsson, Ö.: Dual isotope characterization of total organic carbon in wintertime  
522 carbonaceous aerosols for northern India. *J. Geophys. Res.* 121, doi: 10.1002/2016JD024880,  
523 2016.

524 Billmark, K.A., Swap, R.A., Macko, S.A.: Stable isotope and GC/MS characterization African  
525 aerosols. *South African J. Sci.* 101, 177-170, 2005.

526 Birch, M.E., Cary, R.A.: Elemental carbon-based method for monitoring occupational exposures  
527 to particulate diesel exhaust. *Aerosol Sci. Technol* 25, doi: 10.1080/02786829608965393, 1996.

528 Bird, M.I., Cali, J.A.: A million-year record of fire in sub-Saharan Africa. *Nature* 394, 767-769,  
529 doi: 10.1038/29507, 1998.

530 Blanchard, D.C., Woodcock, A. H.: The production, concentration, and vertical distribution of the  
531 sea-salt aerosol. *Annal. N.Y. Acad. Sci.* doi: 10.1111/j.1749-6632.1980.tb17130.x, 1980.

532 Bond, T.C., Doherty, S.J., Fahey, D.W., Forster, P.M., Berntsen, T., DeAngelo, B.J., Flanner,  
533 M.G., Ghan, S., Kärcher, B., Koch, D., Kinne, S., Kondo, Y., Quinn, P.K., Sarofim, M.C., Schultz,  
534 M.G., Schultz, M., Venkataram, C., Zhang, H., Zhang, S., Bellouin, N., Guttikunda, S.K., Hopke,  
535 P.K., Jacobson, M.Z., Kaiser, J.W., Klimont, Z., Lohmann, U., Schwarz, J.P., Shindell, D.,  
536 Storelvmo, T., Warren, S.G., Zender, C.S.: Bounding the role of black carbon in the climate  
537 system: A systematic assessment. *J. Geophys. Res.* 118, 5380-5552, doi: 10.1002./jgrd.50171,  
538 2013.

539 Brandt, M., Rasmussen, K., Penuelas, Tian, F., J., Schurgers, G., Verger, A., Mertz, O., Palerm,  
540 J.R.B., Fensholt, R.: Human population growth offsets climate-driven increase in woody  
541 vegetation in sub-Saharan Africa. *Nature Ecol. Evol.* 1, doi: 10.1038/s41559-017-0081, 2017.

542 Brito, J., Freney, E., Dominutti, P., Borbon, A., Haslett, S.L., Batenburg, A.M., Colomb, A.,  
543 Dupuy, R., Denjean, C., Burnet, F., Bourriane, T., Deroubaix, A., Sellegri, K., Borrmann, S. Coe,

544 H., Flamant, C., Knippertz, P., Schwarzenboeck, A.: Assessing the role of anthropogenic and  
545 biogenic source on PM<sub>1</sub> over southern West Africa using aircraft measurements. *Atmos. Chem.*  
546 *Phys.* 18, 757-772, doi: 10.5194/acp-18-757-2018, 2018.

547 Cachier, H., Buat-Menard, P., Fontuge, M., Rahnker, J.: Source terms and source strengths of the  
548 carbonaceous aerosol in the tropics. *J. Atmos. Chem.* 3, 469-489, doi: 10.1007/BF00053872, 1985.

549 Cahoon, D.R., Stocks, B.J., Levine, J.S., Cofer III, W.R., O'Neil, K.P.: Seasonal distribution of  
550 African savanna fires. *Nature*, 359, 812-815, doi: 10.1038/359812a0 , 1992.

551 Cais, P., Bombelli, A., Williams, M., Piao, S.L., Chave, J., Ryan, C.M., Henry, M., Brender, P.,  
552 Valentini, R.: The carbon balance of Africa: synthesis of recent research studies. *Phil. Trans. Roy.*  
553 *Soc. A* 369, 2038-2057, doi: 10.1098/rsta.2010.0328, 2011.

554 Das, O., Wang, Y., Hsieh, Y.-P.: Chemical and carbon isotopic characteristics of ash and smoke  
555 derived from burning of C<sub>3</sub> and C<sub>4</sub> grasses. *Org. Geochem.* 41, 263-269,  
556 10.1016/j.orggeochem.2009.11.001, 2010.

557 Dasari, S., Andersson, A., Bikkina, S., Holmstrand, H., Budhavant, K., Sateesh, S., Asmi, E.,  
558 Kesti, J., Backman, J., Salam, A., Singh Bisht, D., Tiwari, S., Hameed, S., Gustafsson, Ö.:  
559 Photochemical degradation affects the light absorption of water-soluble brown carbon in the South  
560 Asian outflow. *Sci. Adv.* 5, doi: 10.1126/sciadv.aau8066, 2019.

561 DeWitt, H.L., Gasore, J., Rupakheti, M., Potter, K.E., Prinn, R.G., Ndikubwimana, JdD., Nkusi,  
562 J., Safari, B.: Seasonal and diurnal variability in O<sub>3</sub>, black carbon, and CO measured at the Rwanda  
563 Climate Observatory. *Atmos. Chem. Phys.* 19, 2063-2078, doi: 10.5194/acp-19-2063-201, 2019.

564 Fang, W., Andersson, A., Zheng, M., Lee, M., Holmstrand, H., Kim, S-W., Du, K., Gustafsson,  
565 Ö.: Divergent evolution of carbonaceous aerosols during dispersal of East Asian haze. *Sc. Rep.* 7,  
566 doi: 10.1038/s41598-017-10766-4, 2017.

567 Formenti, P., Elbert, W., Maenhaut, W., Haywood, J., Osborne, S., Andreae, M.O.: Inorganic and  
568 carbonaceous aerosols during the Southern African Regional Science Initiative (SAFARI 2000)

569 experiment: Chemical characteristics, physical properties, and emission data for smoke from  
570 African biomass burning. *J. Geophys. Res.* 108. Doi: 10.1029/2002JD002408, 2003.

571 Gao, S., Hegg, D.A., Hobbs, P.V., Kirchstetter, T.W., Magi, B.I., Sadilek, M.: Water-soluble  
572 organic components in aerosols associated with savanna fires in southern Africa: Identification,  
573 evolution and distribution. *J. Geophys. Res.* 108, doi: 10.1029/2002JD002324, 2003.

574 Gatari, M.J., Boman, J.: Black carbon and total carbon measurements at urban and rural sites in  
575 Kenya, East Africa. *Atmos. Environ.* 8, 1149-1154, doi: 10.1016/S1352-2310(02)01001-4, 2003.

576 Graven, H.: Impact of fossil fuel emissions on atmospheric radiocarbon and various applications  
577 of radiocarbon over this century. *Proc. Nat. Acad. Sci.* 112, 9542-9545, doi:  
578 10.1073/pnas.1504467112, 2015.

579 Gustafsson, Ö., Kruså, M., Zencak, Z., Sheesley, R.J., Granat, L., Engström, E., Praveen, P.S.,  
580 Rao, P.S.P., Leck, C., Rodhe, H.: Brown clouds over South Asia: Biomass or fossil fuel  
581 combustion? *Science* 323, 495-498, doi: 10.1126/science.1164857, 2009.

582 Heft-Neal, S., Burney, J., Bendavid, E., Burke, M.: Robust relationship between air quality and  
583 infant mortality in Africa. *Nature* 559, 254-258, doi: 10.1038/s41586-018-0263-3, 2018.

584 Hodnebrog, Ø., Myhre, G., Forster, P.M., Sillman, J., Samset, B.H.: Local biomass burning is a  
585 dominant cause of the observed precipitation reduction in southern Africa. *Nature Com.* 7, doi:  
586 10.1038/ncomms11236, 2015.

587 IPCC – Inter-Governmental Panel for Climate Change: AR5 Climate Change 2013: The physical  
588 science basis. ISBN 978-1107661820, 2013.

589 IPCC – Inter-Governmental Panel for Climate Change: AR5 Climate Change 2014: Impacts,  
590 adaptation and vulnerability. ISBN 978-1-107-68386-0, 2014.

591 Keeling, C.D.: The concentration and isotopic abundances of atmospheric carbon dioxide in rural  
592 areas. *Geochem. Cosmochim. Acta.* 13, 322-334, doi: 10.1016/0016-7037(58)90033-4, 1958.

593 Kirchstetter, T.W., Novakov, T., Hobbes, P.V., Magi, B.: Airborne measurements of carbonaceous  
594 aerosols in southern Africa during the dry biomass season. *J. Geophys. Res.* 108. Doi:  
595 10.1029/2002JD002171, 2003.

596 Kirillova, E.N., Andersson, A., Sheesley, R.J., Kruså, M., Praveen, P.S., Budhavant, K., Safai,  
597 P.D., Rao, P.S.P., Gustafsson Ö:  $^{13}\text{C}$  and  $^{14}\text{C}$ -based study of sources and atmospheric processing  
598 of water-soluble organic carbon (WSOC) in South Asian aerosols. *J. Geophys. Res.* 118, 621-626,  
599 doi: 10.1002/jgrd.50130, 2013.

600 Kirillova, E.N., Andersson, A., Han, J., Lee, M., Gustafsson, Ö.: Sources and light absorption of  
601 water-soluble organic carbon aerosols in the outflow from northern China. *Atmos. Chem. Phys.*  
602 14, 1413-1422, doi: 10.5194/acp-14-1413-2014, 2014.

603 Kulmala, M.: Build a global Earth Observatory. *Nature* 553, 21-23, 2018.

604 Liousse, C., Assamoi, E., Criqui, C., Rosset, R.: Explosive growth in African combustion  
605 emissions from 2005 to 2030. *Environ. Res. Lett.* 9, doi: 10.1088/1748-9326/9/3/035003, 2014.

606 Lipset-Moore, G.J., Wolff, N., Game, E.T.: Emissions mitigation opportunities for savanna  
607 countries from early dry season fire management. *Nature Com.* 9, doi: 10.1038/s41467-018-  
608 04687-7, 2018.

609 Lloyd, J., Bird, M.I., Vellen, L., Miranda, A.C., Veenendaal, E.M., Djangbletey, G., Miranda, H.S.,  
610 Cook, G., Faruqhar, G.D.: Contributions of woody and herbaceous vegetation to tropical savanna  
611 ecosystem productivity: a quasi-global estimate. *Tree Phys.* 28, 451-468, doi:  
612 10.1093/treephys/28.3.45, 2008.

613 López-Ballesteros, A., Beck, J., Bombelli, A., Grieco, E., Lorenkova, E.K., Merbold, L.,  
614 Brümmer, C., Hugo, W., Scholes, R., Vackar, D., Vermeulen, A., Acosta, M., Butterbach-Bahl,  
615 K., Helmschrot, J., Kim, D.-G., Jones, M., Jorch, V., Pavleka, M., Skjelvan, I., Saunders, M.:  
616 Towards a feasible and representative pan-African research infrastructure network for GHG  
617 observations. *Environ. Res. Lett.* 13, doi: 10.1088/1748-9326/aad66c, 2018.

618 Maenhaut, W., Salma, I., Cafmeyer, J., Annegarn, H.J., Andreae, M.O.: Regional atmospheric  
619 aerosols composition and sources in the eastern Transvaal, South Africa, and impact of biomass  
620 burning. *J. Geophys. Res.* 101, 23631-23650, 1996.

621 **Martens, J., Wild, B., Pearce, C., Tesi, T., Andersson, A., Bröder, L., O'Regan, M.,**  
622 **Jakansson, M., Sköld, M., Gemery, L., Cronin, T.M., Semiletov, I., Dudarev, O.V.,**  
623 **Gustafsson, Ö.: (2019) Remobilization of Old Permafrost Carbon to Chukchi Sea Sediments**

624 **During the End of the Last Deglaciation. *Glob. Biogeochem. Cyc.* 33, 2-14, doi:**  
625 **10.1029/2018GB005969.** Martinelli, L.A., Camargo, P.B., Lara, L.B.L.S., Victoria, R.L., Artaxo,  
626 P.: Stable carbon and nitrogen isotopic composition of bulk aerosol particles in a C<sub>4</sub> plant  
627 landscape of southeast Brazil. *Atmos. Environ.* 36, 2427-2432, doi: 10.1016/S1352-  
628 2310(01)00454-X, 2002.

629 Marwick, T.R., Tamooch, F., Teofuru, C.R., Borget, A.V., Darchambeau, F., Bouillon, S.: The age  
630 of river-transported carbon: global perspective. *Glob. Biogeochem. Cyc.* 29, 122-137, doi:  
631 10.1002/2014GB004911, 2015.

632 Mkoma, S.L., Kawamura, K., Tachibana, E., Fu, P.: Stable carbon and nitrogen isotopic  
633 compositions of tropical atmospheric aerosols: sources and contribution from burning of C<sub>3</sub> and  
634 C<sub>4</sub> plants to organic aerosols. *Tellus B*, 66, 1-12, doi: 10.3402/tellusb.v66.20176, 2014."

635 O'Leary, M.H.: Carbon isotopes in photosynthesis. *Bioscience* 38, 328–36, doi: 10.2307/1310735,  
636 1988.

637 Palmer, P.I., Feng, L., Chevallier, F., Bösch, H., Somkuti, P.: Net carbon emissions from African  
638 biosphere dominate pan-tropical atmospheric CO<sub>2</sub> signal. *Nature Com.* 10. doi: 10.1038/s41467-  
639 019-11097-w, 2019.

640 Puxbaum, H., Rendl, J., Allabashi, R., Otter, L., Scholes, M.C.: Mass balance of the atmospheric  
641 aerosol in a South African savanna (Nylsvley, May 1997). *J. Geophys. Res.* 105, 20697-20706,  
642 2000.

643 Roberts, G.O., Gelman, A., Gilks, W.R.: (1997) Weak convergence and optimal scaling of random  
644 walk Metropolis algorithms. *Ann. Appl. Prob.* 7, 110-120. Sheesley, R.J., Kirillova, E.N.,  
645 Andersson, A., Kruså, M., Praveen, P.S., Budhavant, K., Safai, P.D., Rao, P.S.P., Gustafsson, Ö.:  
646 Year-round radiocarbon-based source apportionment of carbonaceous aerosols at two background  
647 sites in South Asia. *J. Geophys. Res.* 117, doi: 10.1029/2011JD017161, 2012.

648 Sinha, P., Hobbs, P.V., Yokelson, R.J., Bertschi, I.T., Blake, D.R., Simpson, I.J., Gao, S.,  
649 Kirchstetter, T.W., Novakov, T.: Emissions of trace gases and particles from savanna fires in  
650 southern Africa. *J. Geophys. Res.* 108, doi: 10.1029/2002JD002325, 2003.



651 Swap, R.J., Annegard, H.J., Suttles, J.T., King, M.D., Platnick, S., Privette, J.L., Scholes, R.J.:  
652 Africa burning: A thematic analysis of the Southern African regional science initiative (SAFARI  
653 2000). *J. Geophys. Res.* 108, doi: 10.1029/2003JD003747, 2003.

654 Tiitta, P., Vakkari, V., Croteau, P., Beukes, J.P., van Zyl, P.G., Josipovic, M., Venter, A.D., Jaaros,  
655 K., Pienaar, J.J., Ng, N.L., Canagaratna, M.R., Jayne, J.T., Kerminen, V.-K., Kokola, H., Kulmala,  
656 M., Laaksonen, A., Worsnop, D.R., Laakso, L.: Chemical composition, main sources and temporal  
657 variability of PM1 aerosols in southern African grassland. *Atmos. Chem. Phys.* 14, 1909-1927,  
658 doi: 10.5194/acp-14-1909-2014, 2014.

659 Turekian, V. C., Macko, S., Swap, R. J. and Garstang, M.: Causes of bulk carbon and nitrogen  
660 isotopic fractionations in the products of vegetation burns: laboratory studies. *Chem. Geol.* 152,  
661 181-192, 10.1016/S0009-2541(98)00105-3, 1998.

662 Turnbull, J.C., Mikaloff Fletcher, S.E., Ansell, I., Brailsford, G.W., Moss, R.C., Norris, M.W.,  
663 Steinkamp, K.: Sixty years of radiocarbon dioxide measurements at Wellington, New Zealand:  
664 1965-2014. *Atmos. Chem. Phys.* 17, 14771-14784, doi: 10.5194/acp-17-14771-2017, 2017.

665 UNDP – United Nations Development Programme: 2018 Africa Sustainable Development Report:  
666 Towards a transformed and resilient continent. ISBN: 978-92-1-125134-0, 2018.

667 UNEP/WMO – United Nations Environment Programme/World Meteorological Organization:  
668 Integrated assessment of black carbon and tropospheric ozone. ISBN: 978-92-807-3142-2, 2012.

669 Valentini, R., Arneth, A., Bombelli, A., Castaldi, S., Cazzolla Gatti, R., Chevallier, F., Cias, P.,  
670 Grieco, E., Hartmann, J., Henry, M., Houghton, R.A., Jung, M., Kutsch, W.L., Malhi, Y.,  
671 Mayorga, E., Merbold, L., Murray-Tortarolo, G., Papale, D., Peylin, P., Poulter, B., Raymond,  
672 P.A., Santini, M., Sitch, S., Vaglio Laurin, G., van der Werf, G.R., Williams, C.A., Scholes, R.J.:  
673 A full greenhouse gases budget of Africa: synthesis, uncertainties, and vulnerabilities.  
674 *Biogeosciences* 11, 381-407, doi: 10.5194/bg-11-381-2014, 2014.

675 WHO – World Health Organization: Health effects of black carbon. ISBN: 978 92 890 0265 3,  
676 2012.

677 WHO – World Health Organization: Ambient air pollution: A global assessment of exposure and  
678 burden of disease. ISBN: 9789241511353, 2016.

679 Widory, D.: Combustibles, fuels and their combustion products: A view through carbon isotopes.  
680 Combust. Theory Mod. 10, 831-841, doi: 10.1080/13647830600720264, 2006.

681 Wild, B., Andersson, A., Bröder, L., Vonk, J., Hugelius, G., McClelland, J.W., Song, W.,  
682 Raymond, P.A., Gustafsson, Ö.: Rivers across the Siberian Arctic unearth the patterns of carbon  
683 release from thawing permafrost. Proc. Nat. Acad. 116, 10280-10285, doi:  
684 10.1073/pnas.1811791116, 2019.

685 Williams, C.A., Hanan, N.P., Neff, J.C., Scholes, R.J., Berry, J.A., Denning, S.A., Baker, D.F.:  
686 Africa and the global carbon cycle. Carbon Bal. Manag. 2, 1-13, doi: 10.1186/1750-0680-2-3,  
687 2007.

688 **Winiger, P., Andersson, A., Eckhardt, S., Stohl, A., Semiletov, I.P., Dudarev, O.V., Charkin,**  
689 **A., Shakova, N., Klimont, Z., Heyes, C., Gustafsson, Ö.: (2017) Siberian Arctic black carbon**  
690 **sources constrained by model and observation. Proc. Nat. Acad. Sci. doi:**  
691 **10.1073/pnas.1613401114.** Winiger, P., Barrett, T.E., Sheesley, R.J., Huang, L., Sharma, S.,  
692 Barrie, L.A., Yttri, K.E., Evangeliou, N., Eckhardt, S., Stohl, A., Klimont, Z., Heyes, C.,  
693 Semiletov, I.P., Dudarev, O.V., Charkin, A., Shakhova, N., Holmstrand, H., Andersson, A.,  
694 Gustafsson, Ö.: Source apportionment of circum-Arctic atmospheric black carbon from isotopes  
695 and modelling. Sci. Adv. 5, doi: 10.1126/sciadv.aau8052, 2019.

696 Yan, C., Zheng, M., Bosch, C., Andersson, A., Desyaterik, Y., Sullivan, A.P., Collett, J.L., Zhao,  
697 B., Wang, S., He, K., Gustafsson, Ö.: Important fossil source contribution to brown carbon in  
698 Beijing during Winter. Sci. Rep. 7, doi: 10.1038/srep43182, 2017.

699 **TABLES**

700 **Table 1.** Concentrations of carbonaceous aerosol ( $\mu\text{gC m}^{-3}$ ) and inorganic ions ( $\mu\text{g m}^{-3}$ ) in fine  
 701 aerosols from ground-based and airborne measurements over Sub-Saharan Africa (bkg =  
 702 background).

Sampling site	TC	OC	BC/EC	WSOC	$\text{NO}_3^-$	$\text{SO}_4^{2-}$	$\text{NH}_4^+$	$\text{K}^+$
RCO, dry <sup>a</sup>	9.5±3.7	8.2±3.2	1.3±0.6	5.7±2.1	1.2±0.7	2.1±1.0	0.8±0.3	0.7±0.3
RCO, wet <sup>a</sup>	2.4±1.2	2.2±1.1	0.20±0.1	1.5±0.7	0.1±0.1	0.7±0.3	0.3±0.1	0.08±0.05
Rural Tanzania, dry <sup>b</sup>	7±2	6±2	1.0±0.3	4±1	0.18±0.06	0.2±0.1	0.9±0.7	1.5±0.7
Rural Tanzania, wet <sup>b</sup>	4±1	4±1	0.5±1.3	3±1	0.06±0.03	0.1±0.1	0.2±0.1	0.4±0.2
Aircraft, Southern Africa, smoke <sup>c</sup>	N/A	N/A	N/A	N/A	4.84±0.02	10.4±0.6	N/A	13.1±0.1
Aircraft, Southern Africa, bkg <sup>c</sup>	N/A	N/A	N/A	N/A	0.48±0.00	2.2±0.1	N/A	0.31±0.02
Aircraft, Southern Africa fresh <sup>d</sup>	N/A	20±18	2±1	N/A	1.4±1.8	1.9±1.4	1.6±2.4	4.5±8.1
Aircraft, Southern Africa aged <sup>d</sup>	N/A	6±3	1.03±0.04	N/A	1.0±0.8	2.0±1.5	0.9±0.8	0.6±0.4
Aircraft, Southern Africa, plume <sup>e</sup>	106±86	91±74	15±12	N/A	N/A	N/A	N/A	N/A
Aircraft, Southern Africa haze <sup>e</sup>	10.5±8.2	9.5±6.8	2.3±1.8	N/A	N/A	N/A	N/A	N/A
Aircraft, Southern Africa <sup>f</sup>	8.5±4.8	N/A	2.3±1.9	N/A	0.8±0.3	4.5±3.6	N/A	0.4±0.1
National Park, South Africa <sup>g</sup>	N/A	N/A	1.2 - 2.2	N/A	N/A	N/A	N/A	0.22 - 0.34
Savanna, South Africa <sup>h</sup>	9.1	N/A	0.61	N/A	0.4	11.08	2.85	0.28
Aircraft, W. Africa, bkg <sup>i</sup>	N/A	N/A	0.33 – 0.35	N/A	0.11 – 0.12	1.64 – 1.70	0.63 – 0.68	N/A
Aircraft, W. Africa, urban plume <sup>i</sup>	N/A	N/A	0.64 – 0.72	N/A	0.49 – 0.53	2.70 – 3.03	1.20 – 1.38	N/A
Grassland, South Africa, dry <sup>j</sup>	N/A	N/A	0.6	N/A	0.3	1.4	0.2	N/A
Grassland, South Africa, wet <sup>j</sup>	N/A	N/A	0.3	N/A	0.2	0.4	0.3	N/A
Savanna, South Africa, spring <sup>k</sup>	N/A	N/A	0.40	N/A	0.05	2.48	0.05	0.17
Savanna, South Africa, summer <sup>k</sup>	N/A	N/A	0.16	N/A	0.01	5.65	0.01	0.2

703 a. Present study

704 b. Mkoma et al., 2014

705 c. Gao et al., 2003

706 d. Formenti et al., 2003

707 e. Kirchstetter et al, 2003

708 f. Sinha et al., 2003

709 g. Maenhaut et al., 1996

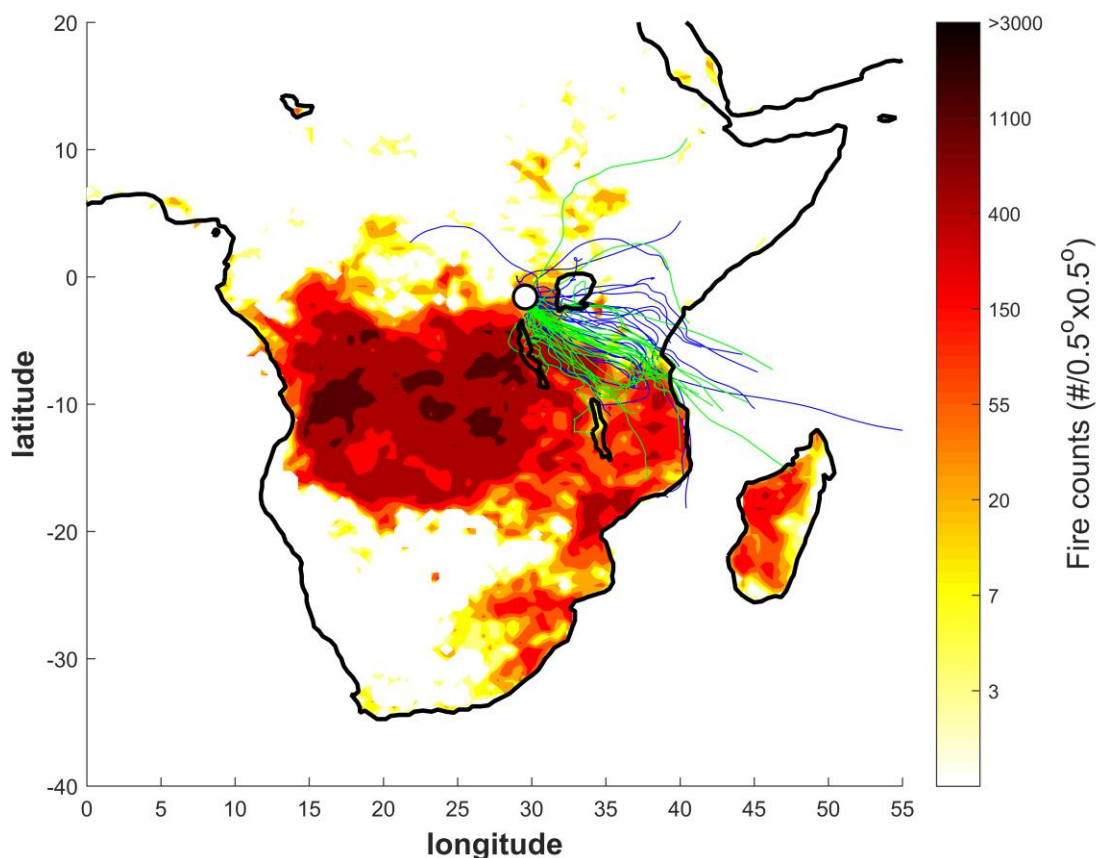
710 h. Puxbaum et al., 2000

711 i. Brito et al., 2018

712 j. Tiitta et al., 2014

713 k. Aurela et al., 2016

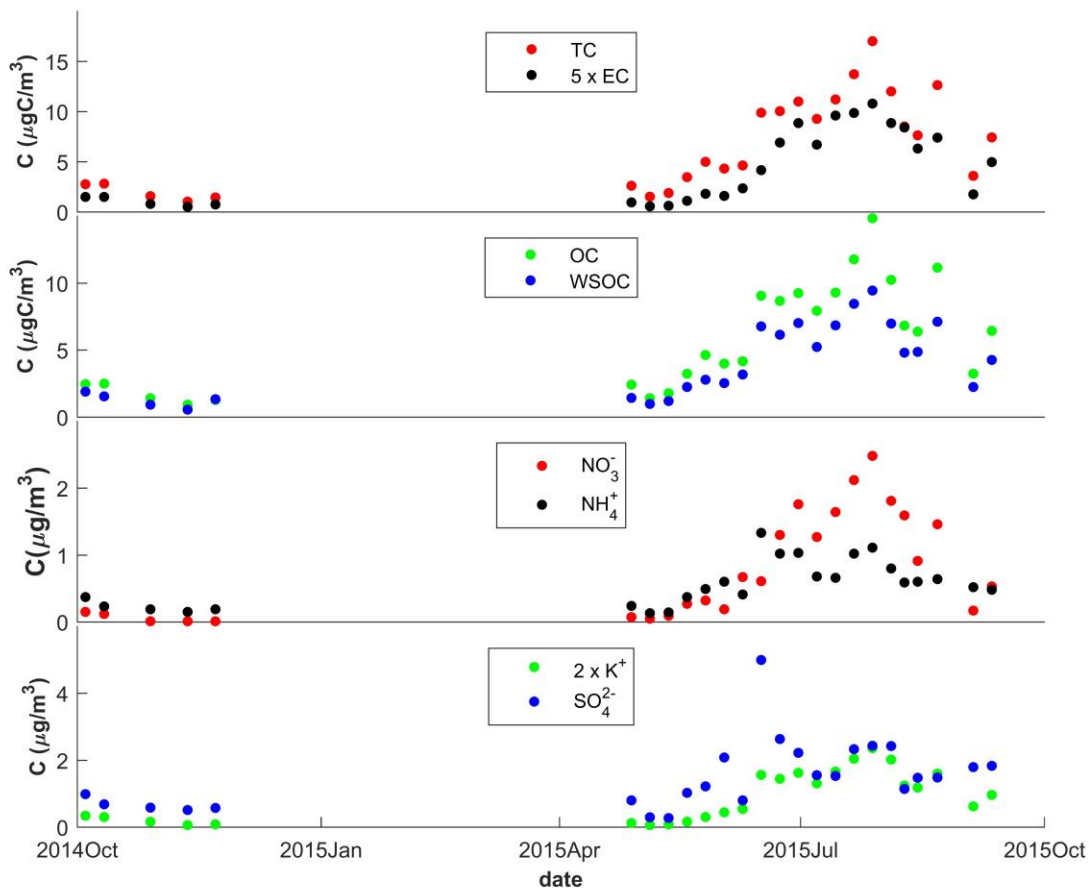
714 **FIGURES**



715  
716 **Figure 1** Fire counts and air mass back trajectories for the October 2014 to September 2015  
717 campaign at the Rwanda Climate Observatory (RCO, black and white circle). The fire counts are  
718 from the Fire Information for Resource Management System (FIRMS) derived from the NASA  
719 Moderate Resolution Imaging Spectroradiometer (MODIS) satellite product for June-July-August  
720 (JJA), 2015. The thin lines represent (4AM, C.A.T.) 5-day air mass back-trajectories arriving at  
721 RCO 100 m.a.g.l. (2690 m.a.s.l.). The blue lines correspond to what we here refer to as the ‘wet’  
722 seasons (October-November 2014 and April-May 2015), whereas the green lines represent the dry  
723 JJA season.

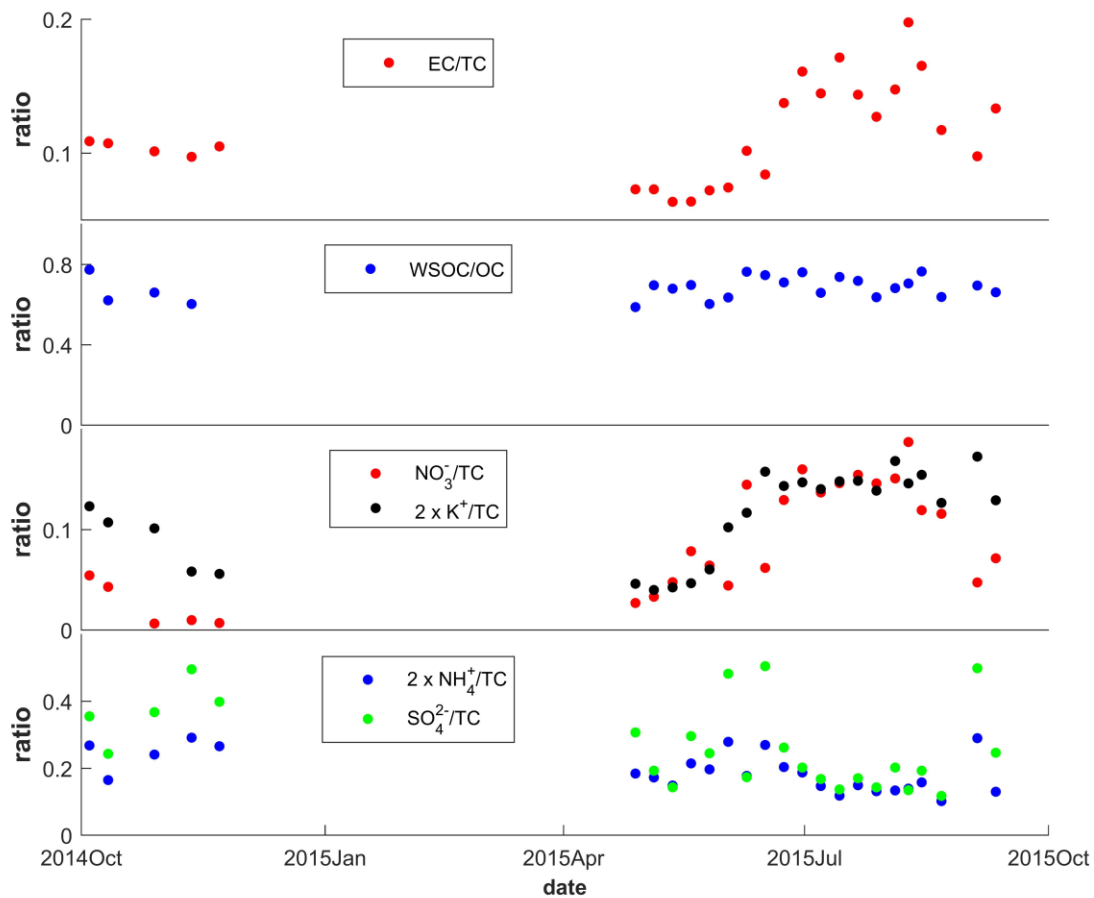
724

725



726

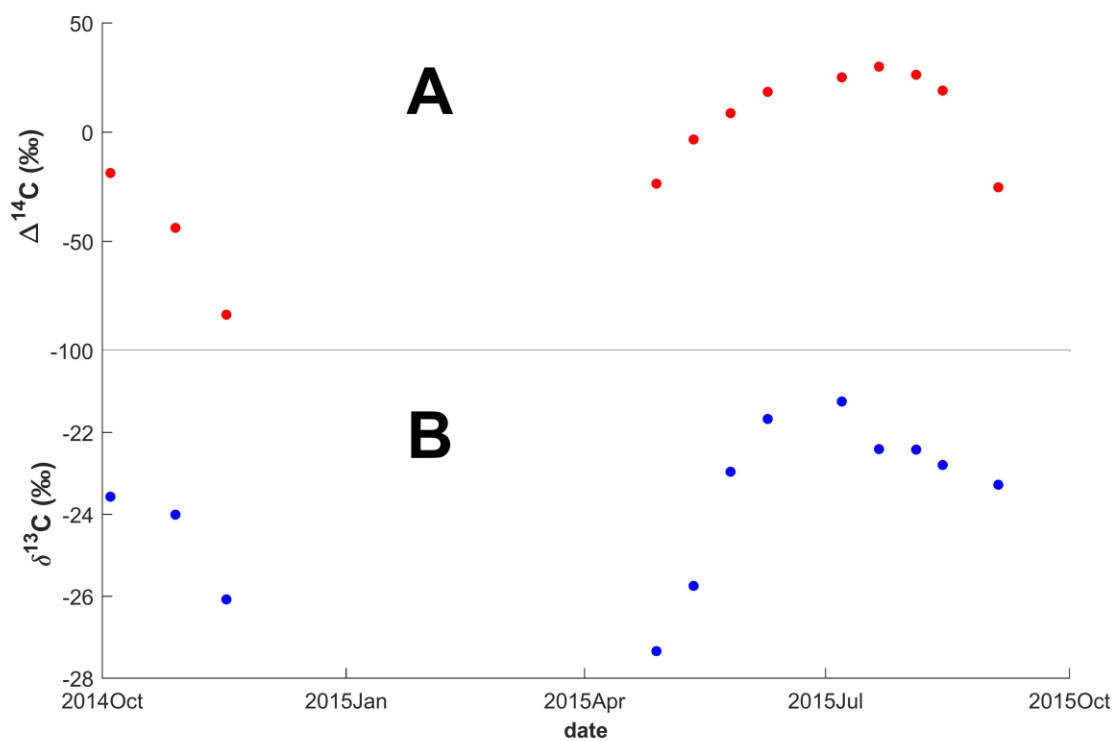
727 **Figure 2.** Concentrations of carbonaceous aerosols (TC = total carbon; EC = elemental carbon;  
 728 OC = organic carbon; WSOC = water-soluble organic carbon) and inorganic ions in PM<sub>2.5</sub> during  
 729 October 2014 to September 2015 at the Rwanda Climate Observatory. Instruments were hit by  
 730 lightning resulting in a data gap November 2014 to April 2015. The concentrations of EC were  
 731 multiplied by 5 and K<sup>+</sup> by 2 for visual clarity.



732

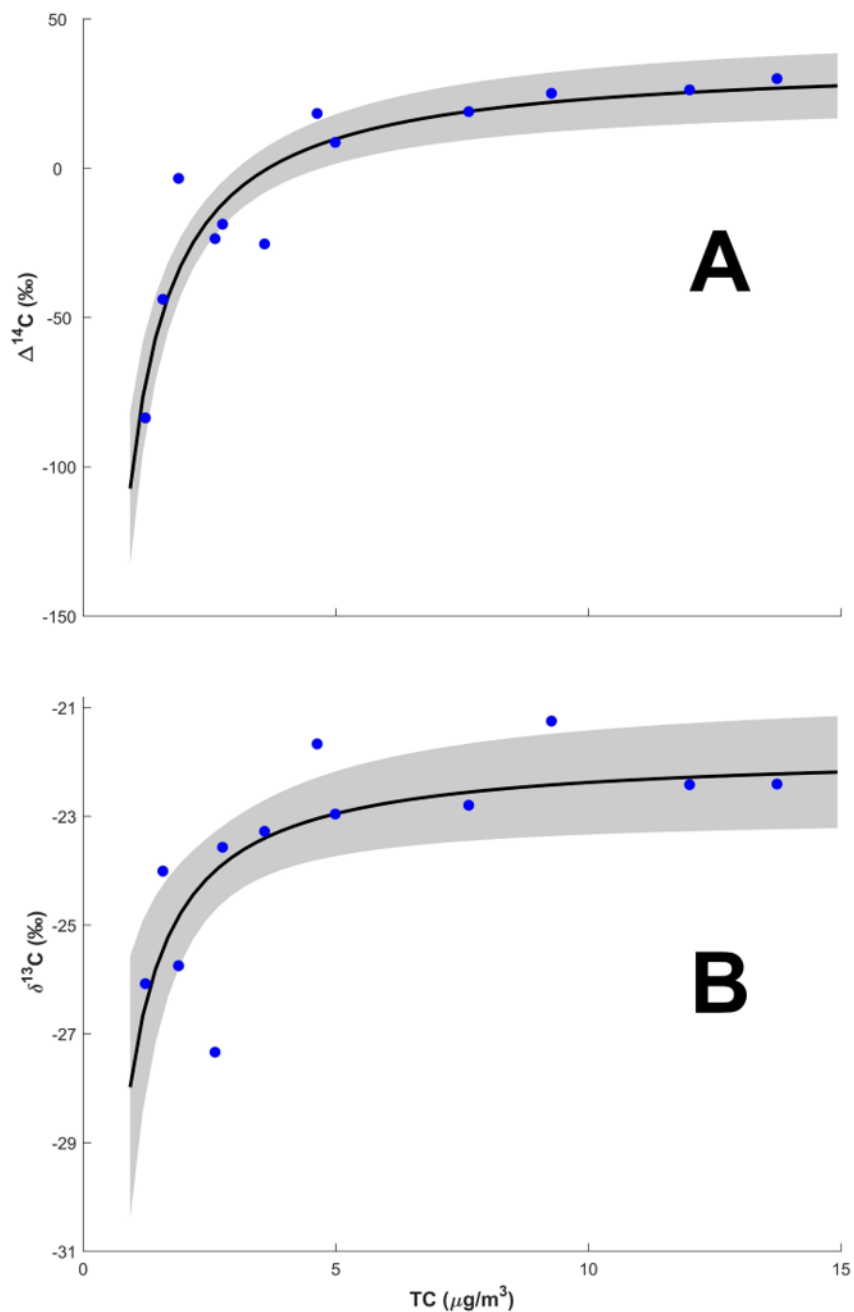
733 **Figure 3.** Ratios of carbonaceous aerosols (EC = elemental carbon; OC = organic carbon; WSOC  
 734 = water-soluble organic carbon) and inorganic ions relative to total carbon (TC) in PM<sub>2.5</sub> during  
 735 October 2014 to September 2015 at the Rwanda Climate Observatory. Instruments were hit by  
 736 lightning resulting in a data gap November 2014 to April 2015. The concentrations of K<sup>+</sup>/TC and  
 737 NH<sub>4</sub><sup>+</sup>/TC ratios were multiplied by 2 for visual clarity.

738



739

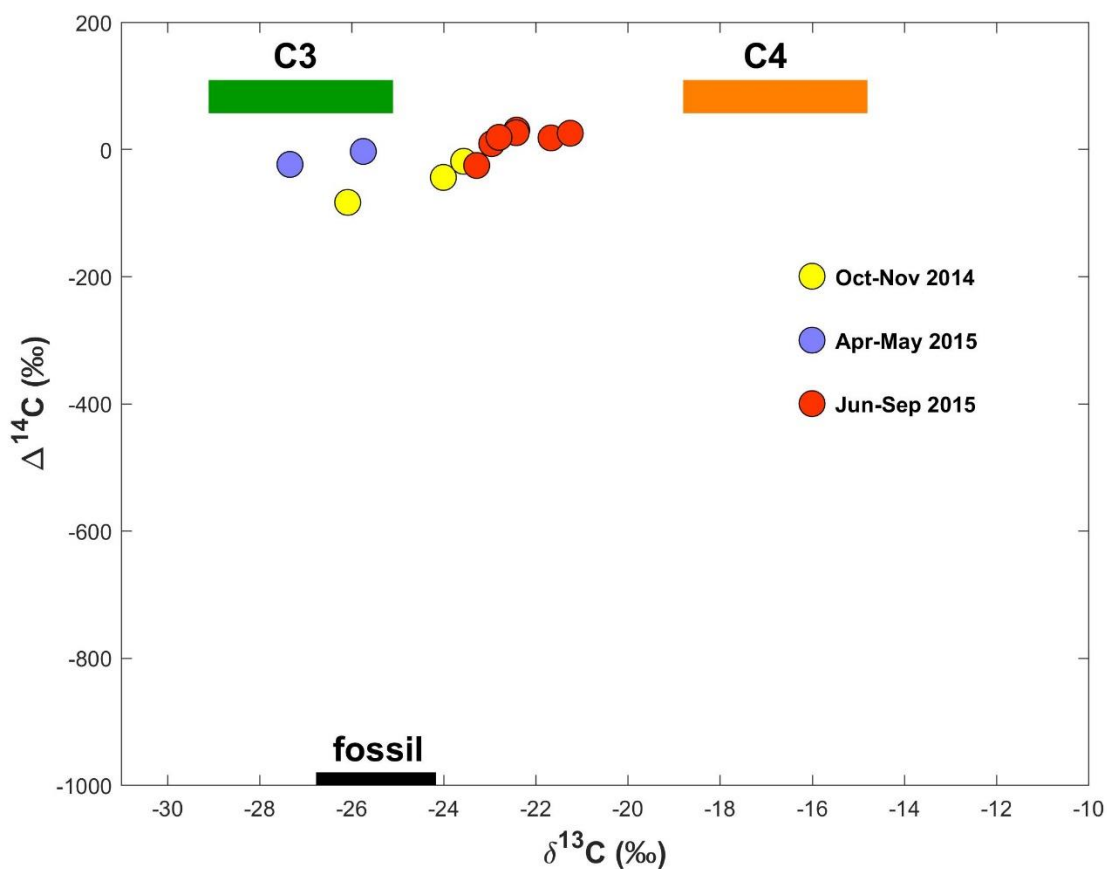
740 **Figure 4:** Dual carbon isotope data for TC vs time. Panel A.  $\Delta^{14}\text{C}$  and Panel B.  $\delta^{13}\text{C}$ . The  
 741 uncertainties for  $\Delta^{14}\text{C}$  are below 50‰ and  $\sim 0.2$ ‰ for  $\delta^{13}\text{C}$ . Instruments were hit by lightning  
 742 resulting in a data gap November 2014 to April 2015.



743

744 **Figure 5.** Interrelations of carbon isotope signatures and TC (blue circles). Panel A.  $\Delta^{14}\text{C}$  vs TC,  
 745 Panel B.  $\delta^{13}\text{C}$  vs TC. The black line is the mean fit of the equation  $\Delta^{14}\text{C}, \delta^{13}\text{C} = A/[\text{TC}] + B$ , using  
 746 Markov chain Monte Carlo simulations, where A and B are fitting parameters. For  $\Delta^{14}\text{C}$ ,  $A = -$   
 747  $135 \pm 16 \text{ } \text{‰} \mu\text{g m}^{-3}$ ;  $B = 37 \pm 6 \text{ } \text{‰}$ . For  $\delta^{13}\text{C}$ ,  $A = -5.8 \pm 1.5 \text{ } \text{‰}$ ;  $B = -21.8 \pm 0.6 \text{ } \text{‰} \mu\text{g m}^{-3}$ . The grey  
 748 shaded area display the  $1\sigma$  spread of the fit.





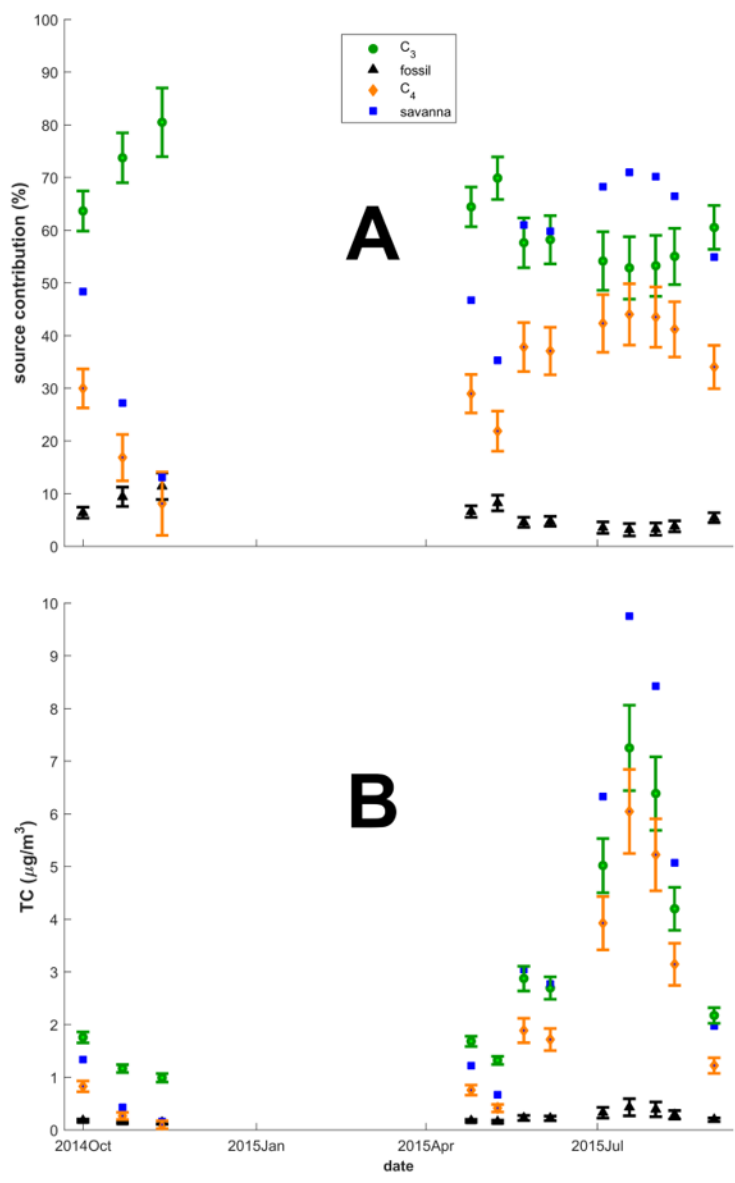
749

750 **Figure 6:** Dual carbon ( $\Delta^{14}\text{C}$  vs  $\delta^{13}\text{C}$ ) isotope plot of TC. Blue circles represent Oct-Nov 2014  
 751 (wet), yellow circles Apr-May 2015 (wet), and red circles Jun-Sept 2015 (dry). The boxes  
 752 represent the endmember ranges (mean  $\pm$  stdev; see Section 3.5 for details) of the three main  
 753 sources: C<sub>3</sub>-plants (green), C<sub>4</sub>-plants (orange), and fossil (black).

754

755

756



757

758 **Figure 7:** Carbon isotope source-segregated fractions and concentrations of TC vs time computed  
 759 with the 'best endmember scenario'. Panel A. Relative source contributions (%) of C<sub>3</sub>-plants  
 760 (green circles), C<sub>4</sub>-plants (orange diamonds) and fossil (black triangles). Estimated savanna  
 761 contributions are shown as blue squares. Panel B. Source segregated concentrations of TC of C<sub>3</sub>-  
 762 plants (green circles), C<sub>4</sub>-plants (orange diamonds) and fossil (black triangles). The error bars  
 763 (standard deviations) were calculated using Markov chain Monte Carlo simulations.

764